THE JOURNAL OF PHYSICAL CHEMISTRY C

Article

pubs.acs.org/JPCC

Effect of Alkyl Chain Length on Hygroscopicity of Nanoparticles and Thin Films of Imidazolium-Based Ionic Liquids

Amanda C. MacMillan, Theresa M. McIntire, Scott A. Epstein, and Sergey A. Nizkorodov*

Department of Chemistry, University of California, Irvine, California 92697-2025, United States

Supporting Information

ABSTRACT: This work focuses on the interaction of water vapor with ionic liquids (ILs) consisting of $[C_nMIM]^+$ (n = 2, 4, or 6) cations paired with Cl^- or BF_4^- anions to examine the effect of alkyl chain length on IL hygroscopicity. Tandem nanodifferential mobility analysis (TDMA) and attenuated total reflectance-Fourier transform infrared (ATR-FTIR) spectroscopy were used to study IL nanoparticles and thin films. Studying IL nanoparticles overcomes kinetic limitations potentially present in bulk experiments as true IL−water vapor equilibrium is quickly established. Growth curves recorded in TDMA experiments showed steady uptake of water vapor with increasing RH. ILs containing Cl^- absorbed more water than those containing BF_4^- over the entire RH range, and IL hygroscopicity decreased with increasing alkyl chain length. The intensities of water stretching vibrations in IL thin films exposed to water vapor measured with ATR-FTIR were in qualitative agreement with the TDMA measurements. Water molar fractions for IL nanoparticles were calculated, and the performance of several water activity coefficient models were evaluated by fits to the experimental data. These combined experimental and modeling techniques help provide a more complete picture for these two families of ILs in the presence of water.

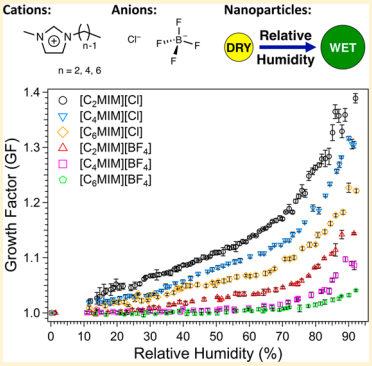

INTRODUCTION

Discovery, design, and utilization of ionic liquids (ILs) in a myriad of applications continue to increase rapidly.[1,2] Uptake of water vapor from ambient air by ILs can dramatically alter their physical and chemical properties, affecting applications in which the ILs are utilized.[1,2] Scores of studies have examined the interaction of imidazolium-based ILs with water (for a list of studies regarding the uptake of water by imidazolium-based ILs, see MacMillan et al.[3] and references therein), yet quantitative data describing the amount of atmospheric water vapor ILs can absorb is lacking. Furthermore, the majority of previous IL−water vapor equilibrium studies examined bulk quantities of ILs.[4−6] Water vapor uptake by bulk quantities of ILs may take several hours or longer to reach equilibrium and can even lead to uncertainty in whether equilibrium was ever reached.[4−6]

Seeking to circumvent the limitations associated with studying bulk imidazolium-based ILs, in our previous work we studied the interaction of water vapor with nanoparticles and thin films of 1-ethyl-3-methylimidazolium chloride ($[C_2MIM][Cl]$) and 1-ethyl-3-methylimidazolium tetrafluoroborate ($[C_2MIM][BF_4]$).[3] We performed nanoparticle hygroscopic growth measurements (the first application of this technique to ILs), attenuated total reflectance-Fourier transform infrared (ATR-FTIR) spectroscopy measurements, and molecular dynamics (MD) simulations of IL−water mixtures. Equilibrium with water vapor was achieved in less than a second for IL nanoparticles (20−30 nm in diameter) and less than 30 min for IL thin films (thickness of a few micrometers) due to absence of mass transfer limitations typically present in bulk solutions. We confirmed that $[C_2MIM][Cl]$ was more hygroscopic than $[C_2MIM][BF_4]$ over the entire relative humidity (RH) range studied (from ∼0 to 92% RH). Furthermore, hygroscopic growth measurements could be quantitatively converted into equilibrium vapor pressure of water above IL−H_2O mixtures as a function of water molar fraction in the mixture.

In this report, we have extended our previous study to imidazolium-based ILs with longer alkyl chains (i.e., butyl and hexyl) paired with either Cl^- or BF_4^- anions. By aerosolizing ILs, exposing them to humidified air over a broad range of RH, and comparing their wet size to their initial dry size, the amount of water taken up by the particles can be quantitatively determined. In a parallel set of experiments, the nature of the interactions between ILs and water in the vapor phase is examined by ATR-FTIR measurements. ATR-FTIR spectra of $[C_4MIM][Cl]$, $[C_6MIM][Cl]$, $[C_4MIM][BF_4]$, and $[C_6MIM][BF_4]$ thin films exposed to humidified nitrogen were measured, and the C−H and O−H band positions and intensities were determined as a function of RH. Equilibrium molar fractions of water (χ_w) for IL nanoparticles were calculated from hygroscopic growth factors (GFs) and the performance of several one- and two-parameter correlative water activity coefficient models were evaluated to fit the experimental data. These combined experimental and modeling techniques help provide a more comprehensive picture of the behavior of absorbed water in imidazolium-based ILs. The techniques also provide a quantitative

Special Issue: John C. Hemminger Festschrift

Received: March 27, 2014
Revised: June 5, 2014
Published: June 6, 2014

parametrization of the amount of water vapor that ILs with different alkyl chain lengths can absorb under equilibrium conditions.

EXPERIMENTAL METHODS

Materials. This study examined ILs containing $[C_nMIM]^+$ (1-*n*-alkyl-3-methylimidazolium) cations with varying linear alkyl chain lengths (n = 4 or 6) (Figure 1a) that were paired with either chloride (Cl^-) or tetrafluoroborate (BF_4^-) anions (Figure 1b). In addition, we extended results for n = 2 ILs

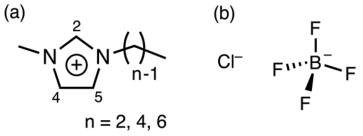

Figure 1. ILs used in this study: (a) 1-*n*-alkyl-3-methylimidazolium ($[C_nMIM]^+$) cations with varying linear alkyl chain lengths (n = 2, 4, or 6) were paired with either (b) a chloride (Cl^-) or tetrafluoroborate (BF_4^-) anion.

previously reported[3] and include them here for comparison with n = 4 and 6 ILs. All ILs were purchased and their sources and purities were as follows: 1-butyl-3-methylimidazolium chloride ($[C_4MIM][Cl]$) (Aldrich 98%), 1-hexyl-3-methylimidazolium chloride ($[C_6MIM][Cl]$) (IoLiTec 98%), 1-butyl-3-methylimidazolium BF_4 ($[C_4MIM][BF_4]$) (Aldrich 98%), and 1-hexyl-3-methylimidazolium BF_4 ($[C_6MIM][BF_4]$) (IoLiTec 99%). To keep the ILs free of water during preparation, all samples were prepared in a drybox that was continuously purged with dry air. After preparation, all chemicals were sealed with paraffin film and stored in a desiccator when not in use. To prevent potential photodegradation, glassware used for purification and drying of $[C_4MIM][BF_4]$ and $[C_6MIM][BF_4]$ was wrapped in foil. In addition, the pure chemicals and prepared solutions were stored in amber vials.

IL Purification. ILs were further purified and dried using established techniques.[1,7−9] $[C_4MIM][Cl]$ and $[C_6MIM][Cl]$ were washed several times (∼4) with ethyl acetate (Acros Organics 99.5% Spectroscopy grade) and dried under rough vacuum (2−3 Torr) at ∼363 K for 48 h. $[C_4MIM][BF_4]$ and $[C_6MIM][BF_4]$ were stirred with activated carbon (Sigma-Aldrich, 20−40 mesh) for 12 h, filtered with a short column of neutral, activated alumina (Fischer, 60−325 mesh), and dried under rough vacuum (2−3 Torr) at ∼343 K for 48 h.

^{1}H NMR Spectroscopy. ILs were monitored before and after purification and drying with ^{1}H NMR spectroscopy using a Bruker DRX500 equipped with a TCI cryoprobe at 298 K using acetone-d_6 (Cambridge Isotope Laboratories, Inc.; D, 99.9% with 1% v/v TMS) as the solvent.

IL Water Content. The amount of water that remained in the ILs after vacuum drying was measured using a Karl Fischer titrator (Mettler Toledo, model DL39) with analyte hydranal coulomat A and catholyte hydranal coulomat CG (both from Fluka). $[C_4MIM][Cl]$ and $[C_6MIM][Cl]$ were prepared by diluting ∼0.6 g of the IL into ∼1 mL of anhydrous methanol (MeOH). Anhydrous MeOH was prepared by sparging with argon and then dried with columns that contained Q-5 and molecular sieves. For $[C_4MIM][BF_4]$ and $[C_6MIM][BF_4]$, neat samples were inspected. The water contents of $[C_4MIM][Cl]$, $[C_6MIM][Cl]$, $[C_4MIM][BF_4]$, and $[C_6MIM][BF_4]$, an average of 3−4 measurements of the solutions and neat samples, were ∼526, ∼278, ∼99, and ∼168 ppm, respectively, by mass. The water content of the anhydrous MeOH solvent was ∼180 ppm using Karl Fischer titration.

IL Nanoparticle Generation and Hygroscopic Growth Factor Measurements. Experimental procedures used for preparation of IL solutions for electrospray, generation of IL nanoparticles, and measurement of the hygroscopic GFs using tandem nanodifferential mobility analysis (TDMA) have been described in detail elsewhere.[3] Briefly, IL solutions were electrosprayed and dried to generate a polydisperse aerosol of IL. Using a nanodifferential mobility analyzer (nano-DMA) operated under dry conditions (<1% RH) at 295 K, a narrrow size distribution of nanoparticles was selected from the initial polydisperse aerosol. Dry particles were exposed to humidified air at a contolled RH, leading to their increase in size. The size distribution of the humidified particles was measured with a second nano-DMA operated at the same RH used for particle humdification, and the humidified particles were counted using a condensation particle counter.

FTIR Spectroscopy Measurements. Experimental procedures used for preparation of IL solutions for FTIR, preparation of ATR crystals, and spectroscopy measurement of water vapor uptake by IL films have been described in detail elsewhere.[3] Briefly, a solution of $[C_4MIM][Cl]$ was prepared for FTIR by dissolving the purified and dried solid IL in anhydrous MeOH (final solution concentration of ∼0.5 g L^{-1}; to resemble the solutions used for ES). Purified and dried liquid $[C_6MIM][Cl]$, $[C_4MIM][BF_4]$, and $[C_6MIM][BF_4]$ were used neat. To remove solvent and/or water absorbed during film preparation, IL-coated ATR crystals were dried overnight in the ATR cell with a flow of dry nitrogen (UHP). ATR-FTIR measurements were conducted at 295 K.

RESULTS AND DISCUSSION

Hygroscopic Growth of IL Nanoparticles. Figure 2 shows the measured hygroscopic growth curves (from ∼0 to 92% RH) for $[C_4MIM][Cl]$, $[C_6MIM][Cl]$, $[C_4MIM][BF_4]$, and $[C_6MIM][BF_4]$ nanoparticles. Our previous results for $[C_2MIM][Cl]$ and $[C_2MIM][BF_4]$ are also included for comparison.[3] Under dry conditions, all six ILs had initial mobility-equivalent diameters ($d_{m,dry}$) of 26.9 ± 0.1 nm. Full and size-selected particle mobility distributions for $[C_4MIM][Cl]$, $[C_6MIM][Cl]$, $[C_4MIM][BF_4]$, and $[C_6MIM][BF_4]$ are provided in the Supporting Information (Figures S1−S4). Exposing the particles to a well-defined RH causes the particles to uptake water vapor and increase in size. In these experiments, the mobility-equivalent diameters of the wet particles ($d_{m,wet}$) in equilibrium with water vapor are measured at different RH values. The amount of water uptake by the IL particles is quantified by the GF (eq 1).

$$\mathrm{GF}\ (\mathrm{RH}) = \frac{d_{\mathrm{m,wet}}(\mathrm{RH})}{d_{\mathrm{m,dry}}} \qquad (1)$$

Growth curves are obtained by plotting the measured GF (eq 1) as a function of RH.

The hygroscopicity aerosol measurements were time-consuming; a single day typically provided a data set spanning 10−30% RH units. These individual experimental runs were then compiled to construct the growth curves for each IL. All GF values were averaged into 3% RH bins; each bin contained ≥7 measurements from several independent experimental runs. These measurements were highly reproducible as indicated by the 95% confidence intervals shown in Figure 2. At RH

dx.doi.org/10.1021/jp503049j | J. Phys. Chem. C 2014, 118, 29458−29466

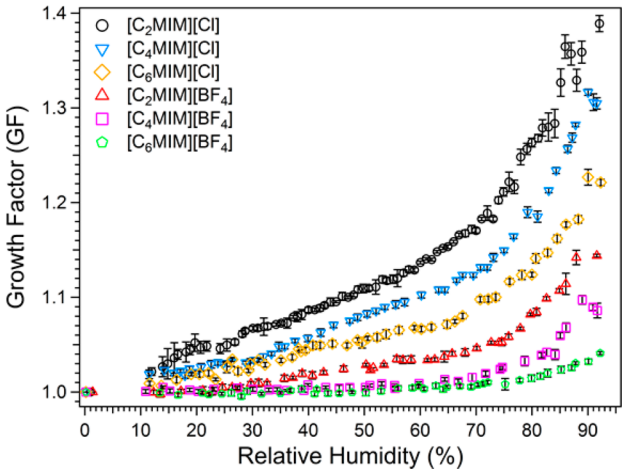

Figure 2. Hygroscopic growth curves of mobility equivalent diameter selected 26.9 ± 0.1 nm particles of $[C_4MIM][Cl]$ (blue inverted triangles), $[C_6MIM][Cl]$ (yellow diamonds), $[C_4MIM][BF_4]$ (pink squares), and $[C_6MIM][BF_4]$ (green pentagons). IL growth curve data from our previous study[3] of $[C_2MIM][Cl]$ (black circles) and $[C_2MIM][BF_4]$ (red triangles) are included for comparison. All ILs exhibit a gradual increase in GF as the RH is increased. ILs containing Cl^- anions have larger GFs compared to those containing BF_4^- anions because they take up more water. The amount of absorbed water goes down as the size of the alkyl chain in the ILs increases.

values >85%, data became less reproducible because of the increased sensitivity of RH to temperature at these values (the RH error bars are not shown in Figure 2, but they increase at higher RH). There are no data from ∼1−10% RH because this RH range is difficult to achieve with our TDMA setup.

In these experiments, nanoparticles were exposed to a specific RH for ∼7 s. We ensured that equilibrium was reached on this time scale by performing additional experiments that exposed the IL nanoparticles to a specific RH for ∼70 s. The GF values did not change with the increased interaction time. This suggests that the equilibration time was very short, in agreement with the expected fast diffusion of water molecules through IL nanoparticles. For example, using diffusion coefficient data for water in various $[C_4MIM][BF_4]$−water mixtures,[10] water is expected to diffuse through a 26.9 nm $[C_4MIM][BF_4]$ nanoparticle in microseconds.

As shown in Figure 2, all IL growth curves exhibit a gradual increase in GF as the RH increases. Over the entire RH range, as the alkyl chain length of the $[C_nMIM][Cl]$ and $[C_nMIM][BF_4]$ (n = 2, 4, or 6) ILs increases, there is a noticeable decrease in GF (Figure 2). Furthermore, all three $[C_nMIM][Cl]$ ILs have larger GFs compared to the three $[C_nMIM][BF_4]$ ILs, and thus the $[C_nMIM][Cl]$ ILs appear to take up more water (a more quantitative analysis of water uptake accounting for differences in densities of droplets will be given below). At the highest RH values measured for the six ILs (∼92%), the GFs of $[C_2MIM][Cl]$, $[C_4MIM][Cl]$, $[C_6MIM][Cl]$, $[C_2MIM][BF_4]$, $[C_4MIM][BF_4]$, and $[C_6MIM][BF_4]$ are 1.39 ± 0.01, 1.30 ± 0.01, 1.22 ± 0.01, 1.14 ± 0.01, 1.09 ± 0.01, and 1.04 ± 0.01, respectively. These values correspond to an increase in particle volume from water uptake by a factor of 2.69, 2.20, 1.82, 1.49, 1.30, and 1.12, respectively.

A number of inorganic, ionic compounds have well-defined deliquescence phase transitions that manifest themselves as an abrupt change in the GF at a specific RH value on their hygroscopic growth curves. $[C_2MIM][Cl]$ and $[C_4MIM][Cl]$ have melting points above room temperature, and they could be expected to deliquesce at a certain RH. However, in our previous study, we noted the absence of a deliquescence phase transition for $[C_2MIM][Cl]$.[3] Likewise, $[C_4MIM][Cl]$ also showed no sign of deliquescence transition in its growth curve. These observations could be interpreted in one of three ways. (1) Water is capable of permeating through solid IL nanoparticles resulting in their gradual expansion and eventual dissolution, without a visible volume change. (2) Even trace amounts of water present in solid ILs make them liquid. (3) Solid IL nanoparticles formed during the electrospray process may actually behave as supercooled liquid droplets. The rapid solvent evaporation of MeOH from the electrosprayed droplets, slow nucleation of the IL crystals, and small size of the droplets may not allow enough time for crystallization in the evaporating droplets. From visual observations made in our lab, allowing $[C_2MIM][Cl]$ and $[C_4MIM][Cl]$ to be exposed to ambient air on a lab bench will result in both ILs to uptake water vapor and liquify. The other four ILs are liquid at room temperature, and thus we would not expect to observe a deliquescence phase transition in their growth curves, which is borne out by the observations.

ATR-FTIR Spectra of ILs. The infrared spectra of purified, dry $[C_4MIM][Cl]$, $[C_6MIM][Cl]$, $[C_4MIM][BF_4]$, and $[C_6MIM][BF_4]$ on ZnSe ATR crystals are shown in Figures 3a, 4a, 5a, and 6a, respectively. The spectra are calculated as $-\log(S/S_0)$, where S_0 is the single beam intensity through the clean ZnSe ATR crystal and S is the beam intensity through the ATR crystal coated with a layer of dry IL. IR spectra of these ILs have been collected in multiple studies[3,11−26] and have been assigned. Spectral bands in the region from 3200 to 3000 cm^{-1} are attributed to the coupled aromatic C−H stretching vibrations of the imidazolium ring, while those between 3000 and 2850 cm^{-1} can be assigned to the aliphatic C−H stretches of

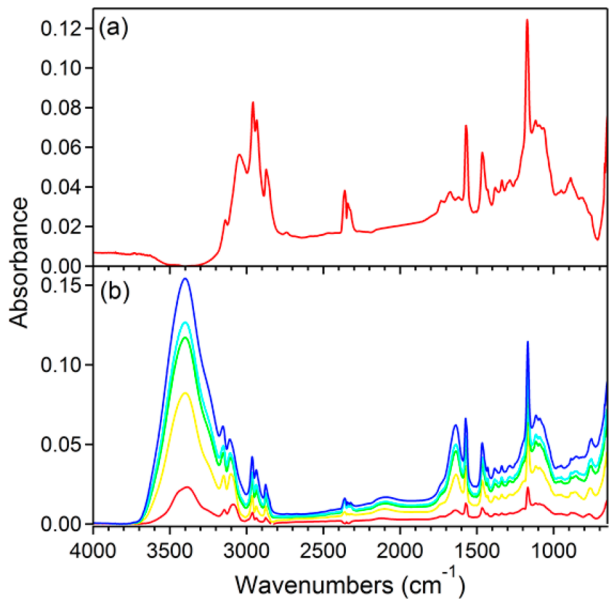

Figure 3. (a) ATR-FTIR spectra of dry $[C_4MIM][Cl]$ on ZnSe. (b) Changes in ATR-FTIR spectra of $[C_4MIM][Cl]$ after exposure to RH values of 3, 36, 62, 72, and 84% (larger RH values correspond to the more intense O−H stretching bands). The spectra after water absorption onto $[C_4MIM][Cl]$ were corrected by subtracting the spectrum of the dry $[C_4MIM][Cl]$.

dx.doi.org/10.1021/jp503049j | J. Phys. Chem. C 2014, 118, 29458−29466

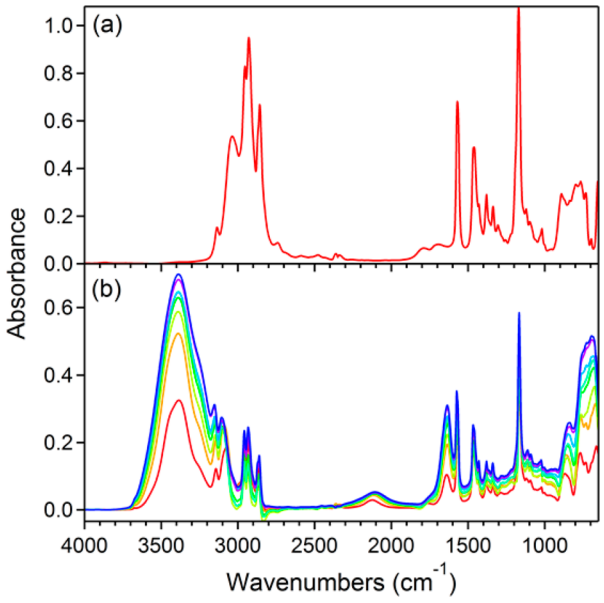

Figure 4. (a) ATR-FTIR spectra of dry $[C_6MIM][Cl]$ on ZnSe. (b) Changes in ATR-FTIR spectra of $[C_6MIM][Cl]$ after exposure to RH values of 4, 18, 43, 48, 57, 63, 80, and 84% (larger RH values correspond to the more intense O−H stretching bands). The spectra after water absorption onto $[C_6MIM][Cl]$ were corrected by subtracting the spectrum of the dry $[C_6MIM][Cl]$.

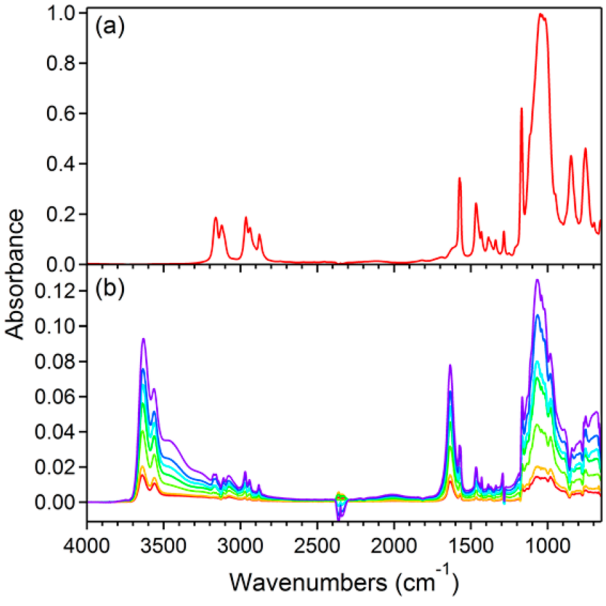

Figure 5. (a) ATR-FTIR spectra of dry $[C_4MIM][BF_4]$ on ZnSe. (b) Changes in ATR-FTIR spectra of $[C_4MIM][BF_4]$ after exposure to RH values of 11, 15, 32, 46, 57, 67, and 82% (larger RH values correspond to the more intense O−H stretching bands). The spectra after water absorption onto $[C_4MIM][BF_4]$ were corrected by subtracting the spectrum of the dry $[C_4MIM][BF_4]$.

the CH_2 and CH_3 groups of the butyl and hexyl chains, and the CH_3 group bonded directly to the $[C_nMIM]^+$ ring.[11−17]

In the spectra of the dry $[C_4MIM][Cl]$ and $[C_6MIM][Cl]$ (Figures 3a and 4a, respectively), the band at 3040 and 3041 cm^{-1}, respectively, is the so-called "Cl^- interaction band" characteristic of stretching vibrations of C4−H (or C5−H) and C2−H interacting with the Cl^- anion.[14,19,20] The dry $[C_4MIM][BF_4]$ and $[C_6MIM][BF_4]$ spectra (Figures 5a and 6a, respectively)

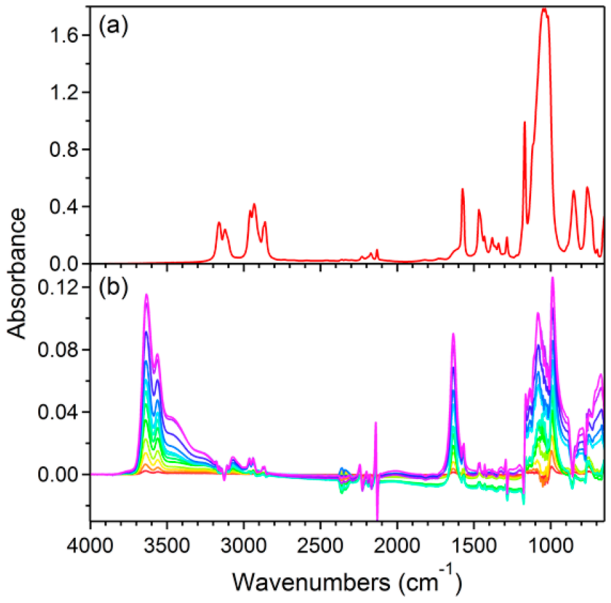

Figure 6. (a) ATR-FTIR spectra of dry $[C_6MIM][BF_4]$ on ZnSe. (b) Changes in ATR-FTIR spectra of $[C_6MIM][BF_4]$ after exposure to RH values of 2, 4, 9, 15, 24, 31, 36, 40, 48, 64, 77, and 81% (larger RH values correspond to the more intense O−H stretching bands). The spectra after water absorption onto $[C_6MIM][BF_4]$ were corrected by subtracting the spectrum of the dry $[C_6MIM][BF_4]$.

exhibit two well-resolved aromatic C−H stretching bands at 3164 and 3118 cm^{-1} (Figure 5a) and at 3161 and 3125 cm^{-1} (Figure 6a). These bands are attributed to hydrogen bonding between BF_4^- and C4−H (or C5−H) and C2−H, respectively.[17,21]

Prominent imidazolium ring stretching modes are seen at 1569 and 1172 cm^{-1} for $[C_4MIM][Cl]$ (Figure 3a),[14] 1568 and 1170 cm^{-1} for $[C_6MIM][Cl]$ (Figure 4a),[14] 1572 and 1170 cm^{-1} for $[C_4MIM][BF_4]$ (Figure 5a),[11] and 1572 and 1170 cm^{-1} for $[C_6MIM][BF_4]$ (Figure 6a).[11] Stretching modes of the BF_4^- anion are the broad peak centered at ∼1049 cm^{-1} (Figure 5a) and ∼1059 cm^{-1} (Figure 6a) and the sharp peaks around 1285 and 753 cm^{-1} (Figure 5a) and 1285 and 759 cm^{-1} (Figure 6a).[11]

Although imidazolium-based ILs containing longer-chained alkyl groups are less miscible with water compared to those containing shorter alkyl groups, these ILs still readily absorb moisture from the air. The extent of water absorption was monitored using ATR-FTIR by exposure of $[C_4MIM][Cl]$, $[C_6MIM][Cl]$, $[C_4MIM][BF_4]$, and $[C_6MIM][BF_4]$ ILs to water vapor in the sealed ATR cell as a function of RH at 295 K. Figures 3b, 4b, 5b, and 6b show IR spectra of $[C_4MIM][Cl]$, $[C_6MIM][Cl]$, $[C_4MIM][BF_4]$, and $[C_6MIM][BF_4]$, respectively, deposited on a ZnSe ATR crystal after exposure to increasing RH. These spectra, after water absorption onto the IL, were corrected by subtracting the background contribution from the dry IL from the absorbance spectra of the hydrated sample. Since the refractive index of an IL−H_2O mixture changes as a function of water content, there is an increase in the effective depth of penetration of the evanescent wave. In addition, the sample may spread differently in the ATR window due to the changes in the viscosity and surface tension of the IL−H_2O mixture. Because of these two effects, the intensities of all bands associated with the ILs increased in the presence of water vapor. In addition, new prominent bands associated with water vibrations appeared in the spectrum.

dx.doi.org/10.1021/jp503049j | J. Phys. Chem. C 2014, 118, 29458−29466

The absorption of water by $[C_4MIM][Cl]$ produced a broad O−H peak centered at 3384 cm^{-1} at low RH (3% RH) that blue-shifts to 3399 cm^{-1} as the RH is increased up to 84% RH (Figure 3b), similar to that for bulk liquid water. Other prominent bands from water are recognized as the water bend at 1640 cm^{-1} and a broad band at ∼2102 cm^{-1} assigned to a combination of the bending mode and a far-IR band associated with a librational mode of sterically hindered water molecules.[22] The intensity of these bands increased concomitantly with the increase in the RH of the added water vapor. In addition, the $[C_4MIM]^+$ ring bands at 1571 and 1169 cm^{-1} are slightly blue-shifted and red-shifted, respectively. Blue-shifted aromatic C−H stretching bands also increase with increasing RH. The interaction of water vapor with $[C_6MIM][Cl]$ produced results similar to $[C_4MIM][Cl]$ with a broad O−H peak centered at ∼3377 cm^{-1} at low RH (4% RH) that blue-shifts to 3392 cm^{-1} as the RH is increased to 84% RH (Figure 4b). Additionally, a water bend at 1638 cm^{-1} and a broad band at ∼2112 cm^{-1} also appear as the RH is increased (Figure 4b). $[C_6MIM]^+$ ring bands at 1571 and 1166 cm^{-1} (Figure 4b) are also slightly blue-shifted and red-shifted, respectively.

The interaction of water vapor with $[C_4MIM][BF_4]$ (Figure 5b) at low RH (11% RH) produced a very different O−H region with peaks assigned as the ν_3 asymmetric stretch at 3638 cm^{-1} and the ν_1 symmetric stretch at 3561 cm^{-1} from single water molecules hydrogen bonded by two BF_4^- anions, as observed previously.[17,23−26] At low RH, the interaction of water vapor with $[C_6MIM][BF_4]$ (Figure 6b) exhibited behavior similar to $[C_4MIM][BF_4]$ with peaks in the O−H region assigned as the ν_3 asymmetric stretch at 3639 cm^{-1} and the ν_1 symmetric stretch at 3561 cm^{-1} (at 2% RH).[17,23−26]

As the RH increased to ∼82% for $[C_4MIM][BF_4]$ (Figure 5b), the intensity of the ν_3 symmetric and ν_1 asymmetric O−H stretches increased and shifted to ∼3633 cm^{-1} and ∼3564 cm^{-1}, respectively. At the same time there is growth of a liquid-like water peak at 3454 cm^{-1} and a shoulder at 3262 cm^{-1}, that dominates when water forms a well-ordered hydrogen bonding network as in ice. Other bands from water are recognized as the water bend at 1632 cm^{-1}, and a broad band at ∼2024 cm^{-1} is assigned to a combination of the bending mode and a far-IR band associated with a librational mode of sterically hindered water molecules.[22] Also evident, at higher RH (82% RH) is an increase of ring bands associated with the $[C_4MIM]^+$ cation at 1570 and 1166 cm^{-1}. The increase in water content and the associated blue-shifts in the C−H stretches are indicative of water having an influence on the C−H interactions.[26]

Similar results were observed for $[C_6MIM][BF_4]$ (Figure 6b). The intensity of the ν_3 symmetric and ν_1 asymmetric O−H stretches increased and shifted to ∼3634 cm^{-1} and ∼3563 cm^{-1}, respectively. The growth of a liquid-like water peak was observed at 3482 cm^{-1} and a shoulder at 3256 cm^{-1}. Additionally, a water bend at 1634 cm^{-1} and a broad band at ∼2017 cm^{-1} also appeared as the RH was increased (Figure 6b). At higher RHs, ring bands associated with the $[C_6MIM]^+$ cation, at 1572 and 1163 cm^{-1}, also increased.

To more systematically evaluate the effect of alkyl chain length on water uptake of the IL thin films as a function of RH, we calculated the ratio of the peak area of the O−H stretching region to that of the imidazolium aromatic ring stretch in the dry IL spectra for all six ILs (Figure 7). The ring stretch peak, centered at approximately 1572 cm^{-1} in all the dry IL spectra, was chosen because it is dominated by the motion of the C═C bonds of the imidazolium ring, which should not be strongly affected by the increase in the alkyl chain length or addition of water. Therefore, this normalization should provide a good metric for the relative amount of water uptake for each of the ILs; a larger ratio value indicates that more water is taken up by the ILs. It should be noted that $[C_4MIM][Cl]$ was omitted from Figure 7 because the low intensity of the dry IL spectrum resulted in unreliable O−H/aromatic peak area ratios compared to the remaining ILs.

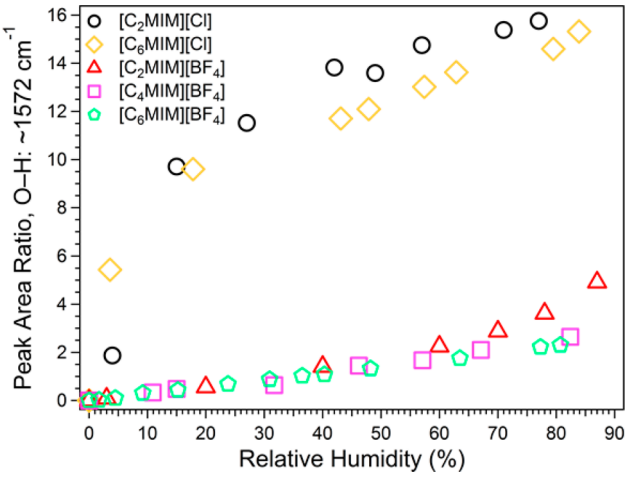

Figure 7. Peak area ratio of the O−H stretching region to the ∼1572 cm^{-1} imidazolium ring stretch in the dry IL spectra as a function of RH. Reanalyzed IL ATR-FTIR data from our previous study,[3] $[C_2MIM][Cl]$ (black circles) and $[C_2MIM][BF_4]$ (red triangles) are included for comparison. ILs containing Cl^- anions have larger O−H/aromatic peak areas compared to those containing BF_4^- anions. As the alkyl chain length of the cation is increased, the O−H/aromatic peak area decreases. $[C_4MIM][Cl]$ was omitted because of low absorbance in the dry IL spectrum.

The $[C_nMIM][Cl]$ ILs have a considerably larger O−H/aromatic peak area ratio compared to the $[C_nMIM][BF_4]$ ILs (Figure 7). Part of the increase may be due to higher O−H stretching band intensities in the Cl^--based ILs, but the majority of the increase reflects higher hygroscopicity of $[C_nMIM][Cl]$ ILs compared to $[C_nMIM][BF_4]$ ILs. As the alkyl chain length of the cation decreases, the O−H/aromatic peak area ratio increases, a trend consistent with the hygroscopic growth measurements. We note that Jeon et al. performed ATR-FTIR measurements on various $[C_4MIM][BF_4]$-H_2O mixtures and plotted O−H vibrational peak areas versus molar water concentration of the solutions.[17] Unfortunately, we are unable to directly compare our results to theirs because our molar water concentrations are significantly smaller.

Equilibrium Molar Fractions of Water in the ILs. As described in our previous work,[3] hygroscopic GFs of the IL nanoparticles can be converted quantitatively into the respective equilibrium molar fractions of water, $\chi_w = n_w/(n_w + n_{IL})$, in the IL−$H_2O$ mixtures using eq 2,

$$\frac{\chi_w}{1-\chi_w} = \left(\frac{MW_{IL}}{MW_w}\right)\left(\frac{\rho_{solution}(\chi_w)}{\rho_{IL}}GF^3 - 1\right) \quad (2)$$

where MW is molecular weight, ρ is density, and the subscripts IL, w, and solution refer to IL, water, and their mixture, respectively. Equation 2 was derived based on the assumption that the nanoparticles are homogeneous spheres and have densities similar to the densities of the corresponding bulk IL−H_2O mixtures (a good assumption for particles this size). In our

dx.doi.org/10.1021/jp503049j | J. Phys. Chem. C 2014, 118, 29458−29466

previous work,[3] we compared χ_w data calculated from water uptake by both nanoparticles and IR thin films and found their χ_w values to be very similar, thus strengthening our argument that nanoparticles can serve as a model system for bulk measurements. For $[C_4MIM][Cl]$, $[C_6MIM][Cl]$, and all three $[C_nMIM][BF_4]$ (n = 2, 4, or 6) ILs, eq 2 was solved numerically for χ_w for every measured GF by using a fit of $\rho_{solution}$ data from Yang et al.,[27] Gomez et al.,[28] and Rilo et al.,[29] respectively, to an empirical dependence on χ_w. For example, χ_w of $[C_4MIM][Cl]$, $[C_6MIM][Cl]$, $[C_2MIM][BF_4]$, $[C_4MIM][BF_4]$, and $[C_6MIM][BF_4]$ nanoparticles at 83% RH was 0.878 ± 0.001, 0.848 ± 0.004, 0.725 ± 0.004, 0.569 ± 0.024, and 0.414 ± 0.049, respectively.

For $[C_2MIM][Cl]$, literature data for its physical properties are scarce. Therefore, in our previous paper,[3] we simplified eq 2 by assuming zero excess volume in the mixture (i.e., additive volumes).

$$\frac{\chi_{w,ideal}}{1-\chi_{w,ideal}} = \left(\frac{MW_{IL}}{MW_w}\right)\left(\frac{\rho_w}{\rho_{IL}}\right)(GF^3 - 1) \quad (3)$$

Both eqs 2 and 3 were used to calculate χ_w for $[C_4MIM][Cl]$, $[C_6MIM][Cl]$, and the $[C_nMIM][BF_4]$ ILs. Equation 3 appears to be a reasonable alternative to the more accurate eq 2 for $[C_4MIM][Cl]$, $[C_6MIM][Cl]$, and the $[C_nMIM][BF_4]$ ILs because it produces almost the same results. For example, at 83% RH $\chi_{w,ideal}$ for $[C_4MIM][Cl]$, $[C_6MIM][Cl]$, $[C_2MIM][BF_4]$, $[C_4MIM][BF_4]$, and $[C_6MIM][BF_4]$ was 0.875 ± 0.002, 0.846 ± 0.004, 0.739 ± 0.004, 0.578 ± 0.024, and 0.428 ± 0.048, respectively; these values are very close to those cited in the previous paragraph. The [Cl] IL-H_2O mixtures do not behave ideally—they exhibit significant deviations from Raoult's law over the entire RH range measured (Figure 8). However, the zero excess volume approximation (eq 3) appears to work well for such mixtures for the purposes of converting hygroscopic growth data into χ_w.

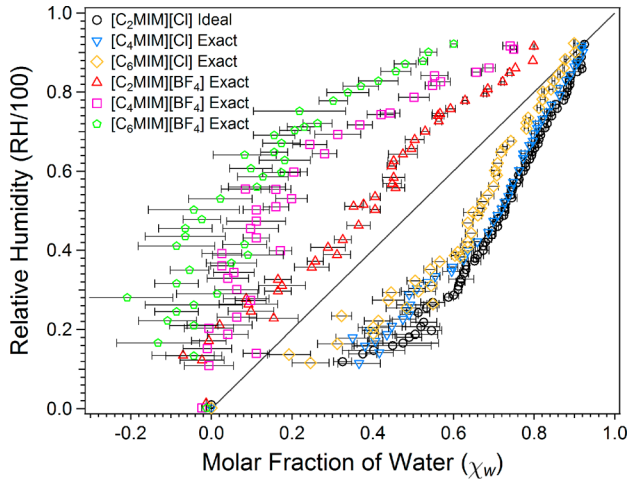

Figure 8. Water activity (RH/100) as a function of the molar fraction of water (χ_w) calculated from the GF values using eq 2 (actual densities) and eq 3 (ideal solution approximation). χ_w data from our previous study,[3] $[C_2MIM][Cl]$ (black circles) and $[C_2MIM][BF_4]$ (red triangles), are included for comparison. Raoult's Law for an ideal solution is represented by the dark gray, solid line.

The dependence of χ_w (for $[C_4MIM][Cl]$, $[C_6MIM][Cl]$, and the $[C_nMIM][BF_4]$ ILs) and $\chi_{w,ideal}$ (for $[C_2MIM][Cl]$) in the IL nanoparticles as a function of RH is shown in Figure 8. The dependence of $\chi_{w,ideal}$ in the IL nanoparticles as a function of RH for $[C_4MIM][Cl]$, $[C_6MIM][Cl]$, and the $[C_nMIM][BF_4]$ ILs can be found in the Supporting Informatin (Figure S5). In order to discuss the dependence in terms of Raoult's law, RH values are purposely placed on the y-axis. Molar water fraction values were not corrected for the Kelvin effect (an increase in the equilibrium vapor pressure of water over the droplet relative to the vapor pressure of water over bulk solution) because the effect is small in nanoparticles of this size (<8% for a ~27 nm water droplet). The Kelvin effect becomes even smaller for IL−H_2O droplets because they have lower surface tension, which decreases when the IL solution concentration or the alkyl chain length is increased

Disregarding the Kelvin effect, the RH/100 values correspond to the equilibrium water activity in the IL−H_2O mixture.[3] The ILs containing the same anion (i.e., either Cl^- or BF_4^-) exhibit qualitatively similar behavior in terms of deviations from Raoult's Law. All $[C_nMIM][BF_4]$ ILs exhibit positive deviations, with the magnitude of the deviation increasing as the alkyl chain length increases. The positive sign of the deviations suggests that the strength of the $[C_nMIM][BF_4]$−water interactions are weaker than the average of the strengths of the water−water and IL−IL interactions. Furthermore, as the length of the alkyl chain increases, the disparity in the interactions grows. These observations are qualitatively consistent with the increased level of hydrophobicity of the $[C_nMIM]^+$ cation for larger n values. These weak interactions are also consistent with the narrow widths and small red-shifts of the O−H stretching bands in the ATR-FTIR spectra of these two ILs (shown in Figures 5 and 6 for $[C_4MIM][BF_4]$ and $[C_6MIM][BF_4]$).

$[C_nMIM][Cl]$−water mixtures all exhibit significant negative deviations from Raoult's Law (Figure 8). Since the cation is the same as in the corresponding $[C_nMIM][BF_4]$ ILs, this suggest much stronger interaction between water and Cl^- versus water and BF_4^-. These results are consistent with strongly red-shifted and broad O−H stretching bands in the IR spectra of all $[C_nMIM][Cl]$−water mixtures examined here and in our previous study.[3] The negative deviations for $[C_2MIM][Cl]$ are large; however, as the alkyl chain length increases up to hexyl ($[C_6MIM][Cl]$), the negative deviations are less significant, suggesting that the interaction strength between water and Cl^- decreases with increasing alkyl chain length.

Additionally, when comparing the $[C_nMIM][Cl]$ ILs and $[C_nMIM][BF_4]$ ILs in Figure 8, the alkyl chain length appears to matter more for $[C_nMIM][BF_4]$ than $[C_nMIM][Cl]$. We believe this is because the type of anion present in the IL has the dominant effect on water uptake and the χ_w present in the IL nanoparticles. The interaction strength between water and Cl^- is much larger than the interaction strength between water and BF_4^-, as shown in our previous MD simulations.[3] This larger interaction strength results in the differences between the χ_w values for the $[C_nMIM][Cl]$ ILs to be much smaller than the $[C_nMIM][BF_4]$ ILs. The larger differences in the χ_w values for $[C_nMIM][BF_4]$ are a direct indication that the type of cation present is only a secondary factor with regard to water uptake and the χ_w present in the IL nanoparticles.

It should be noted that, for eqs 2 and 3, we calculated χ_w by treating the IL as a single component, i.e., by defining χ_w as $n_w/(n_w + n_{IL})$. However, the cation and anion of the IL can alternatively be treated as separate particles, resulting in a different definition of the molar fraction of water, $\chi'_w = n_w/(n_w + 2n_{IL})$. The two values of the molar fraction of water can

dx.doi.org/10.1021/jp503049j | J. Phys. Chem. C 2014, 118, 29458−29466

be related to each other by means of the following equation (eq 4):

$$\chi'_{w} = \frac{\chi_w}{2 - \chi_w} \tag{4}$$

We replotted χ'_w as a function of RH for all six ILs in Figure S6, Supporting Information. The plot looks qualitatively similar to Figure 8; however, the $[C_nMIM][Cl]$ ILs appear to better obey Raoult's law compared to the $[C_nMIM][BF_4]$ ILs when χ'_w is used as the coordinate. This is consistent with the more intercompatible interactions in the case where H_2O interacts with Cl^- as opposed to BF_4^-.

We evaluated the performance of several correlative liquid activity coefficient models to fit the experimental data. In the case of ideal vapor-phase behavior, equating the fugacity of water in the liquid and vapor phase yields the following expression (eq 5):

$$\chi_w \gamma_w(\chi_w) = \frac{p_w}{p_w^{sat}} = \frac{RH}{100} \tag{5}$$

where p_w and p_w^{sat} are the partial pressure of water and the saturation vapor pressure of water, respectively. Nonideal solution behavior is captured with the activity coefficient of water (γ_w).

We evaluated the following commonly used one- and two-parameter correlative water activity coefficient models:[30] one-constant Margules equation (eq 6), two-constant Margules equation (eq 7), van Larr equation (eq 8), Wilson equation (eq 9), and the Flory–Huggins equation (eq 10).

$$\frac{RH}{100} = \chi_w \exp\left(\frac{A\chi_{IL}^2}{RT}\right) \tag{6}$$

$$\frac{RH}{100} = \chi_w \exp\left(\frac{\alpha\chi_{IL}^2 + \beta\chi_{IL}^3}{RT}\right) \tag{7}$$

$$\frac{RH}{100} = \chi_w \exp\left(\frac{\alpha}{\left[1 + \frac{\alpha}{\beta}\frac{\chi_w}{\chi_{IL}}\right]^2}\right) \tag{8}$$

$$\frac{RH}{100} = \chi_w \exp\left(-\ln(\chi_w + \Lambda_{12}\chi_{IL}) + \chi_{IL}\left[\frac{\Lambda_{12}}{\chi_w + \Lambda_{12}\chi_{IL}} - \frac{\Lambda_{21}}{\Lambda_{21}\chi_w + \chi_{IL}}\right]\right) \tag{9}$$

$$\frac{RH}{100} = \chi_w \exp\left(\ln\frac{\phi_w}{\chi_w} + \left(1 - \frac{1}{m}\right)\phi_{IL} + \chi_{Flory}\phi_{IL}^2\right) \tag{10}$$

For eq 10, χ_{Flory} is the Flory interaction parameter and is not related to the molar fraction of water, $\phi_w = (\chi_w/(\chi_w + m\chi_{IL}))$, $\phi_{IL} = (m\chi_{IL})/(\chi_w + m\chi_{IL}))$, $m = (\nu_{IL}/\nu_w)$, ν_w is molar volume of water, and ν_{IL} is molar volume of IL. Fitting parameters, determined with nonlinear least-squares optimizations, are shown in Table 1. For clarity, only the fitting parameters for χ_w (eq 2) for $[C_4MIM][Cl]$, $[C_6MIM][Cl]$, and the $[C_nMIM][BF_4]$ ILs and $\chi_{w,ideal}$ (eq 3) for $[C_2MIM][Cl]$ are presented. Fitting parameters for χ_w and $\chi_{w,ideal}$ for all ILs can be found in the Supporting Information section (Table S1). To use these

Table 1. Water Activity Coefficient Models Fitting Parameters

	one-constant Margules		two-constant Margules			van Laar			Wilson			Flory–Huggins	
	A/RT	R^2	α/RT	β/RT	R^2	α	β	R^2	Λ_{12}	Λ_{21}	R^2	φ_w	R^2
$[C_2MIM][Cl]$ Ideal	−11035 ± 205	0.990	−14900 ± 376	11125 ± 976	0.996	−2.36 ± 0.12	−4.02 ± 0.05	0.995	4.17 ± 0.10	3.75 ± 0.75	0.994	0.00201 ± 0.01967	0.956
$[C_4MIM][Cl]$ Exact	−7690 ± 310	0.982	−11944 ± 597	10256 ± 1264	0.992	−1.50 ± 0.11	−3.06 ± 0.08	0.992	3.87 ± 0.19	1.34 ± 0.23	0.991	0.299 ± 0.017	0.981
$[C_6MIM][Cl]$ Exact	−5300 ± 269	0.970	−7354 ± 823	4720 ± 1741	0.971	−1.49 ± 0.28	−2.09 ± 0.10	0.971	2.67 ± 0.30	1.61 ± 0.50	0.968	0.601 ± 0.017	0.969
$[C_2MIM][BF_4]$ Exact	2254 ± 172	0.907	3484 ± 790	−1891 ± 1190	0.922	0.528 ± 0.095	1.36 ± 0.26	0.934	1.31 ± 0.25	0.176 ± 0.094	0.934	1.27 ± 0.04	0.898
$[C_4MIM][BF_4]$ Exact	4260 ± 175	0.823	4325 ± 1106	−81 ± 1357	0.824	1.71 ± 0.13	1.734 ± 0.18	0.825	0.314 ± 0.068	0.284 ± 0.084	0.834	1.68 ± 0.10	0.601
$[C_6MIM][BF_4]$ Exact	5030 ± 279	0.624	4490 ± 2109	679 ± 2600	0.616	2.10 ± 0.25	1.94 ± 0.31	0.615	0.181 ± 0.088	0.220 ± 0.124	0.624	2.17 ± 0.11	0.360
average R^2		0.882			0.887			0.889			0.891		0.794
R^2 of $[C_nMIM][Cl]$		0.980			0.987			0.986			0.984		0.969
R^2 of $[C_nMIM][BF_4]$		0.784			0.787			0.791			0.798		0.620

dx.doi.org/10.1021/jp503049j | J. Phys. Chem. C 2014, 118, 29458−29466

fitting parameter in situations when the molar fraction of water is defined as $\chi'_w = n_w/(n_w + 2n_{IL})$, one must first calculate χ_w from χ'_w by reversing eq 4.

For the one-constant Margules equation, the fitting parameter "A" has a simple physical interpretation. Positive and negative values of "A" correspond to positive and negative excess free energy for a binary mixture, respectively. The positive deviation from Raoult's Law for the BF_4^--containing ILs results in positive "A" values which increase in magnitude with the alkyl chain length, implying increasing deviations from the ideal behavior. The Cl^--containing ILs with negative deviations from Raoult's Law have negative values of "A", but in contrast to the BF_4^--containing ILs, the magnitudes of "A" decrease with the alkyl chain length. Of the ILs examined in this work, $[C_2MIM][Cl]$ and $[C_6MIM][BF_4]$ deviate from ideality the most, in two opposing directions.

The performance of each activity coefficient model in representing the $[C_2MIM][Cl]$ data is presented in Figure 9.

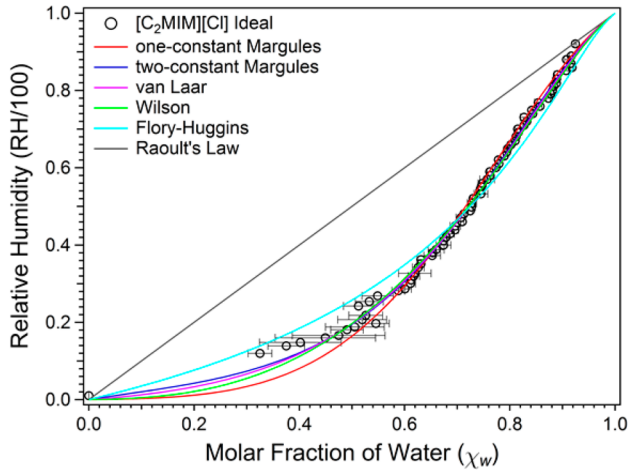

Figure 9. One- and two-parameter correlative water activity coefficient models used to fit the equilibrium molar fractions of water (χ_w) calculated from the IL nanoparticle GF values. $\chi_{w,ideal}$ data for $[C_2MIM][Cl]$ nanoparticles[3] (calculated using eq 3) are used here to represent the performance of each activity coefficient model. The two-parameter equations (i.e., two-constant Margules, van Larr, and Wilson models) performed better than the one-parameter equations (i.e., one-constant Margules and Flory–Huggins models). Raoult's law for an ideal solution is represented by the dark gray, solid line.

Similar plots detailing the other IL–H_2O systems we investigated are shown in the Supporting Information (Figures S7–S16). Overall, all models performed better when describing the behavior of $[C_nMIM][Cl]$ ILs compared to $[C_nMIM][BF_4]$ ILs. But, the two-constant Margules, van Larr, and Wilson models (all two-parameter equations) performed somewhat better than the one-parameter models when describing the behavior of both the $[C_nMIM][Cl]$ ILs and $[C_nMIM][BF_4]$ ILs. Accurately representing the ILs containing BF_4^- anions was considerably more difficult. The Flory–Huggins model, typically used to model polymer systems containing species of dissimilar sizes, requires the liquid molar volumes of the constituents. It then relies on a single fitting parameter to represent the data. The Flory–Huggins model has been used previously to describe a $[C_4MIM][PF_6]$ + water mixture[31] and a $[C_4MIM][BF_4]$ + water mixture.[32] However, with liquid molar volumes from MacMillan et al.[3] as inputs and an empirical fitting parameter designed to scale the enthalpic contribution to the excess Gibbs free energy, this model could not accurately reproduce systems with positive deviations from Raoult's Law. The Flory–Huggins' model performance was especially poor for the BF_4^--containing ILs (see the Supporting Information). Thermodynamic mixing behavior of the IL mixtures containing BF_4^- anions was best represented with the Wilson model. The van Larr and Margules models performed similarly.

CONCLUSION

We have examined the effect of alkyl chain length on IL hygroscopicity for a subset of two families of ILs (i.e., $[C_nMIM][Cl]$ and $[C_nMIM][BF_4]$ (n = 2, 4, or 6)). Using the combined experimental techniques of TDMA hygroscopicity measurements and ATR-FTIR spectroscopy, the results show that all ILs containing Cl^- anions were more hygroscopic than those containing BF_4^- anions over the entire RH range and that uptake of water vapor decreases with increasing alkyl chain length on the $[C_nMIM]^+$ cation. The hygroscopicity of the ILs, in the order of the most to least hygroscopic, are as follows: $[C_2MIM][Cl]$, $[C_4MIM][Cl]$, $[C_6MIM][Cl]$, $[C_2MIM][BF_4]$, $[C_4MIM][BF_4]$, and $[C_6MIM][BF_4]$. Overall, all water activity coefficient models performed better to describe the behavior of $[C_nMIM][Cl]$ ILs compared to $[C_nMIM][BF_4]$ ILs. The two-parameter models performed best in describing the behavior of both the $[C_nMIM][Cl]$ ILs and $[C_nMIM][BF_4]$ ILs.

ASSOCIATED CONTENT

Supporting Information

Figures for IL particle-size distributions, additional figures for molar fractions of water vs RH, additional figures for correlative water activity coefficient models, and a table for additional water activity coefficient models fitting parameters are included in the Supporting Information. This material is available free of charge via the Internet at http://pubs.acs.org.

AUTHOR INFORMATION

Corresponding Author

*E-mail: nizkorod@uci.edu. Tel: +1-949-824-1262.

Notes

The authors declare no competing financial interest.

ACKNOWLEDGMENTS

This study was supported by the National Science Foundation Grant CHE-0909227. ACM is grateful to the National Science Foundation for a NSF graduate student fellowship. ACM would like to thank the UCI research groups of Prof. John Hemminger, Prof. Andy Borovik, and Prof. Larry Overman for providing access to their chemicals and instruments.

REFERENCES

(1) *Ionic Liquids in Synthesis*, 2nd ed.; Wasserscheid, P., Welton, T., Eds.; Wiley-VCH: Weinheim, Germany, 2008; Vol. *1*.

(2) Seddon, K. R.; Stark, A.; Torres, M. J. Influence of Chloride, Water, and Organic Solvents on the Physical Properties of Ionic Liquids. *Pure Appl. Chem.* **2000**, *72*, 2275–2287.

(3) MacMillan, A. C.; McIntire, T. M.; Freites, J. A.; Tobias, D. J.; Nizkorodov, S. A. Interaction of Water Vapor with the Surfaces of Imidazolium-Based Ionic Liquid Nanoparticles and Thin Films. *J. Phys. Chem. B* **2012**, *116*, 11255–11265.

(4) Di Francesco, F.; Calisi, N.; Creatini, M.; Melai, B.; Salvo, P.; Chiappe, C. Water Sorption by Anhydrous Ionic Liquids. *Green Chem.* **2011**, *13*, 1712–1717.

(5) Cuadrado-Prado, S.; Dominguez-Perez, M.; Rilo, E.; Garcia-Garabal, S.; Segade, L.; Franjo, C.; Cabeza, O. Experimental Measurement of the Hygroscopic Grade on Eight Imidazolium Based Ionic Liquids. *Fluid Phase Equilib.* **2009**, *278*, 36−40.
(6) Cao, Y.; Chen, Y.; Sun, X.; Zhang, Z.; Mu, T. Water Sorption in Ionic Liquids: Kinetics, Mechanisms and Hydrophilicity. *Phys. Chem. Chem. Phys.* **2012**, *14*, 12252−12262.
(7) Huddleston, J. G.; Visser, A. E.; Reichert, W. M.; Willauer, H. D.; Broker, G. A.; Rogers, R. D. Characterization and Comparison of Hydrophilic and Hydrophobic Room Temperature Ionic Liquids Incorporating the Imidazolium Cation. *Green Chem.* **2001**, *3*, 156−164.
(8) Gomez, E.; Gonzalez, B.; Dominguez, A.; Tojo, E.; Tojo, J. Dynamic Viscosities of a Series of 1-Alkyl-3-Methylimidazolium Chloride Ionic Liquids and their Binary Mixtures with Water at Several Temperatures. *J. Chem. Eng. Data* **2006**, *51*, 696−701.
(9) Ghatee, M. H.; Zolghadr, A. R. Surface Tension Measurements of Imidazolium-Based Ionic Liquids at Liquid-Vapor Equilibrium. *Fluid Phase Equilib.* **2008**, *263*, 168−175.
(10) Murgia, S.; Monduzzi, M.; Lopez, F.; Palazzo, G. Mesoscopic Structure in Mixtures of Water and 1-Butyl-3-Methyl Imidazolium Tetrafluoborate: A Multinuclear NMR Study. *J. Solution Chem.* **2013**, *42*, 1111−1122.
(11) Katsyuba, S. A.; Zvereva, E. E.; Vidis, A.; Dyson, P. J. Application of Density Functional Theory and Vibrational Spectroscopy Toward the Rational Design of Ionic Liquids. *J. Phys. Chem. A* **2007**, *111*, 352−370.
(12) Snyder, R. G.; Strauss, H. L.; Elliger, C. A. Carbon-Hydrogen Stretching Modes and the Structure of n-Alkyl Chains. 1. Long, Disordered Chains. *J. Phys. Chem.* **1982**, *86*, 5145−5150.
(13) MacPhail, R. A.; Strauss, H. L.; Snyder, R. G.; Elliger, C. A. Carbon-Hydrogen Stretching Modes and the Structure of n-Alkyl Chains. 2. Long, All-trans Chains. *J. Phys. Chem.* **1984**, *88*, 334−341.
(14) Tait, S.; Osteryoung, R. A. Infrared Study of Ambient-Temperature Chloroaluminates as a Function of Melt Acidity. *Inorg. Chem.* **1984**, *23*, 4352−4360.
(15) Talaty, E. R.; Raja, S.; Storhaug, V. J.; Dölle, A.; Carper, W. R. Raman and Infrared Spectra and ab Initio Calculations of C2−4MIM Imidazolium Hexafluorophosphate Ionic Liquids. *J. Phys. Chem. B* **2004**, *108*, 13177−13184.
(16) Heimer, N. E.; Del Sesto, R. E.; Meng, Z.; Wilkes, J. S.; Carper, W. R. Vibrational Spectra of Imidazolium Tetrafluoroborate Ionic Liquids. *J. Mol. Liq.* **2006**, *124*, 84−95.
(17) Jeon, Y.; Sung, J.; Kim, D.; Seo, C.; Cheong, H.; Ouchi, Y.; Wawa, R.; Hamaguchi, H. O. Structural Change of 1-Butyl-3-Methylimidazolium Tetrafluoroborate Plus Water Mixtures Studied by Infrared Vibrational Spectroscopy. *J. Phys. Chem. B* **2008**, *112*, 923−928.
(18) Jeon, Y.; Sung, J.; Seo, C.; Lim, H.; Cheong, H.; Kang, M.; Moon, B.; Ouchi, Y.; Kim, D. Structures of Ionic Liquids with Different Anions Studied by Infrared Vibration Spectroscopy. *J. Phys. Chem. B* **2008**, *112*, 4735−4740.
(19) Dieter, K. M.; Dymek, C. J.; Heimer, N. E.; Rovang, J. W.; Wilkes, J. S. Ionic Structure and Interactions in 1-Methyl-3-Ethylimidazolium Chloride-Aluminum Chloride Molten Salts. *J. Am. Chem. Soc.* **1988**, *110*, 2722−2726.
(20) Hitchcock, P. B.; Seddon, K. R.; Welton, T. Hydrogen-Bond Acceptor Abilities of Tetrachlorometalate(II) Complexes in Ionic Liquids. *J. Chem. Soc., Dalton Trans.* **1993**, 2639−2643.
(21) Katsyuba, S. A.; Dyson, P. J.; Vandyukova, E. E.; Chernova, A. V.; Vidiš, A. Molecular Structure, Vibrational Spectra, and Hydrogen Bonding of the Ionic Liquid 1-Ethyl-3-methyl-1H-imidazolium Tetrafluoroborate. *Helv. Chim. Acta* **2004**, *87*, 2556−2565.
(22) Gurnett, B.; Williams, D. Structure of Water and Aqueous Solutions. In *Proceedings of the International Symposium*; Luck, W. A. P., Ed.; Verlag Chemie/Physik Verlag: Weinheim, Germany, 1974; p 206.
(23) Cammarata, L.; Kazarian, S. G.; Salter, P. A.; Welton, T. Molecular States of Water in Room Temperature Ionic Liquids. *Phys. Chem. Chem. Phys.* **2001**, *3*, 5192−5200.
(24) Fazio, B.; Triolo, A.; Di Marco, G. Local Organization of Water and its Effect on the Structural Heterogeneities in Room-Temperature Ionic Liquid/H2O Mixtures. *J. Raman Spectrosc.* **2008**, *39*, 233−237.
(25) Takamuku, T.; Kyoshoin, Y.; Shimomura, T.; Kittaka, S.; Yamaguchi, T. Effect of Water on Structure of Hydrophilic Imidazolium-Based Ionic Liquid. *J. Phys. Chem. B* **2009**, *113*, 10817−10824.
(26) Zhang, L. Q.; Xu, Z.; Wang, Y.; Li, H. R. Prediction of the Solvation and Structural Properties of Ionic Liquids in Water by Two-Dimensional Correlation Spectroscopy. *J. Phys. Chem. B* **2008**, *112*, 6411−6419.
(27) Yang, Q. W.; Zhang, H.; Su, B. G.; Yang, Y. W.; Ren, Q. L.; Xing, H. B. Volumetric Properties of Binary Mixtures of 1-Butyl-3-methylimidazolium Chloride plus Water or Hydrophilic Solvents at Different Temperatures. *J. Chem. Eng. Data* **2010**, *55*, 1750−1754.
(28) Gómez, E.; Calvar, N.; Domínguez, I.; Domínguez, A. Physical Properties of the Ternary Mixture Ethanol + Water + 1-Hexyl-3-Methylimidazolium Chloride at 298.15 K. *Phys. Chem. Liq.* **2006**, *44*, 409−417.
(29) Rilo, E.; Pico, J.; Garcia-Garabal, S.; Varela, L. M.; Cabeza, O. Density and Surface Tension in Binary Mixtures of CnMIM-BF(4) Ionic Liquids with Water and Ethanol. *Fluid Phase Equilib.* **2009**, *285*, 83−89.
(30) Sandler, S. I. *Chemical and Engineering Thermodynamics*; John Wiley & Sons, Inc.: New York, 1999.
(31) Bendová, M.; Wagner, Z.; Moučka, M. Liquid-liquid Equilibrium in a Binary System 1-Butyl-3-Methylimidazolium Hexafluorophosphate + Water: Experiment and Data Correlation. *Int. J. Thermodyn.* **2008**, *11*, 109−114.
(32) Rebelo, L. P. N.; Najdanovic-Visak, V.; Visak, Z. P.; da Ponte, M. N.; Szydlowski, J.; Cerdeirina, C. A.; Troncoso, J.; Romani, L.; Esperanca, J.; Guedes, H. J. R.; et al. A Detailed Thermodynamic Analysis of [C(4)mim][BF4] plus Water as a Case Study to Model Ionic Liquid Aqueous Solutions. *Green Chem.* **2004**, *6*, 369−381.